Chemically controlled growth of porous CeO$_2$ nanotubes for Cr(VI) photoreduction

Junshu Wu, Jinshu Wang*, Yucheng Du, Hongyi Li, Yilong Yang, Xinjian Jia

School of Materials Science and Engineering, Beijing University of Technology, Chaoyang District, Beijing 100124, China

ABSTRACT

A nanowire-directed templating solution-based synthesis strategy was developed to selectively prepare uniform CeO$_2$ nanotubes and heterostructured nanowires by fine-tuning surface chemistry of K$_{1.33}$Mn$_8$O$_{16}$ nanowires. The morphology of CeO$_2$ nanotubes and the decorative growth of solid CeO$_2$ particles on K$_{1.33}$Mn$_8$O$_{16}$ nanowires changed as the concentration of sodium dodecyl benzene sulfonate (SDBS) was altered. The resultant porous CeO$_2$ nanotubes showed excellent water purification performance for oxalic acid-induced photocatalytic reduction of Cr(VI) under UV light irradiation at room temperature. The enhanced ability for Cr(VI) photoreduction on the obtained CeO$_2$ nanotubes were investigated. Our findings provide a new means to chemically controlled growth of CeO$_2$ nanostructures and demonstrate a highly robust and potential material for the purification of Cr(VI) polluted water.

1. Introduction

A growing number of contaminants such as undesirable heavy metal ions and organic chemical compounds are entering water supplies from human activity, making water purification even more challenging [1,2]. Hexavalent chromium (Cr(VI)) is of particular environmental concern due to its toxicity and mobility and is challenging to remove from wastewater. It does not form insoluble compounds in aqueous solutions, and tends to accumulate in living organisms through the food chain, leading to liver damage, pulmonary congestions, vomiting, severe diarrhea, etc. [3]. Cr(III) is less toxic and can be readily precipitated out of solution in the form of Cr(OH)$_3$. A tremendous amount of research is thus conducted to pursue efficient technologies for reducing potentially harmful Cr(VI) contaminants into Cr(III) species with lower cost, less energy, and minimizing the use of chemicals and impact on the environment [4–6]. Photocatalysis technology is a highly appealing green approach for practical applications to produce water with legally- and practically-acceptable levels of toxic chemicals owing to the simplicity of the concept and its technical feasibility by using sunlight as the primary energy source [7–13]. Compared with traditional Cr(VI) reduction treatments, such as sulfur compound reduction, iron salt reduction, electrochemical reduction, bacteria reduction, etc., which generally suffer from large chemical dosage, high cost, and secondary pollution [3], heterogeneous

photocatalysis reduction of Cr(VI) is mainly involved in a clean reductant electron produced by light irradiation, and it has been proved to be a quite attractive, economical and clean strategy to remedy of Cr(VI) pollution [14–16]. Now rapidly emerging metal oxide semiconductor materials capable of photoreduction removal of Cr(VI) are providing unprecedented opportunities for industrial applications and environmental remediation [17–19]. An aspect of particular importance when developing photocatalyst systems for Cr(VI) reduction over metal oxide semiconductor is how to decrease a fast photogenic charge carrier recombination which will annihilate the charge-separated state and will produce wasted energy without giving the possibility of introducing electrons into an external circuit, thus reducing considerably the quantum efficiency of the photochemical Cr(VI) reduction process [20]. One of the best strategies to high-efficiency photoreduction of Cr(VI) in aqueous solution is the use of suitable organic sacrificial agents to modify the photocatalysis system and process in synergistically enhanced procedure under light irradiation. Strong synergistic effect between Cr(VI) and methyl orange [21], 2, 4, 6-trichlorophenol [22], phenol [23], 4-chlorophenol [24], etc., dramatically enhances photosensitized removal efficiencies. However, the toxicity and possible incomplete mineralization of the colorful dyes or colorless aromatic compounds will be a risk of secondary contamination in the treatment of Cr(VI). Thus, at present searching for new protocols for tailoring of metal oxide nanostructures and finding better sacrificial organic agents still remain as a significant challenge and facilitate the investigations of their catalytic mechanism for further practical applications.

* Corresponding author. Tel.: +86 10 6739 1101; fax: +86 10 6739 1101.
E-mail address: wangjsh@bjut.edu.cn (J. Wang).

Ceria (CeO_2) is commonly used as ultraviolet blocking materials, solar cells, catalysts, etc. [25–27]. Besides being a reducible oxide with O_2 storage capacity, when used as catalyst support, it is capable of interacting with electron-rich surface heteroatoms (X = O or N) which are able to adsorb onto the surface via weak coordination and create new electron donor, strengthening UV light absorbance and favoring catalytic reactions [28]. Recently, CeO_2 and CeO_2-based composite nanostructures have been reported to possess immense potential for applications in wastewater treatment due to its biological and chemical inertness, strong oxidizing capability, cyclic usability as well as extended stability against chemical corrosion [29–32]. However, tailoring morphology to generate more active sites, constructing special microstructures to localize the incident light, modulating reaction environment to change the surface property are still the most important factors promoting the practical applications of CeO_2 materials for cleaning water. In this contribution, we reported our progress on nanowire-directed templating solution-based synthesis of uniform CeO_2 nanotubes by fine-tuning $K_{1.33}Mn_8O_{16}$ nanowire surface chemistry in hydrothermal conditions. We noted changes in the morphology of CeO_2 nanotubes and the decorative growth of solid CeO_2 particles on nanowires) as the concentration of sodium dodecyl benzene sulfonate (SDBS) was altered. The resultant CeO_2 nanotubes showed excellent water purification performance for Cr(VI) photoreduction with the assistance of oxalic acid at room temperature.

2. Experimental

2.1. Materials

Potassium permanganate ($KMnO_4$), ammonium fluoride (NH_4F), ammonium sulfate ((NH_4)$_2SO_4$), cerium(III) nitrate hexahydrate ($Ce(NO_3)_3 \cdot 6H_2O$), and potassium dichromate ($K_2Cr_2O_7$) were purchased from Beijing Chemical Reagent Research Company. Sodium dodecyl benzene sulphonate (SDBS), sodium fluoride (NaF), and oxalic acid ($H_2C_2O_4$) were supplied by Sinopharm Chemical Reagent Co., Ltd. Anhydrous ethanol and isopropanol were purchased from Tianjin Fuchen Chemical Reagent Factory. All chemicals used in this study were of commercially available analytical grade and without further purification.

2.2. Preparation of samples

In a typical procedure for the preparation of CeO_2 nanotubes, $K_{1.33}Mn_8O_{16}$ nanowires were firstly prepared with $KMnO_4$, NH_4F, and (NH_4)$_2SO_4$ in hydrothermal conditions (the synthesis process has been described in detail elsewhere) [33]. The synthesized $K_{1.33}Mn_8O_{16}$ nanowires (0.03 g) were dispersed in 10 mL 0.1 M $Ce(NO_3)_3$ aqueous solution containing 0.1 g SDBS. The mixture was transferred into a Teflon-lined 20-mL-capacity stainless steel autoclave followed by sealing the autoclave. The temperature of the electric oven was set at 150–170 °C for 40–45 h. After the autoclave was air-cooled to room temperature, the products were collected, rinsed with absolute ethanol and de-ionized water, and dried at 60 °C for 2–3 h in air. For the synthesis of $K_{1.33}Mn_8O_{16}$ @ CeO_2 nanowires, 0.03 g $K_{1.33}Mn_8O_{16}$ nanowires were dispersed in 10 mL 0.02 M $Ce(NO_3)_3$ aqueous solution, then the mixture was hydrothermally treated in a Teflon-lined 20-mL-capacity stainless steel autoclave at 150–170 °C for 24–26 h.

2.3. Characterization

The as-prepared samples were characterized by X-ray diffraction (XRD) on a SHIMADZU XRD-7000 XRD diffractometer using Cu Kα radiation (λ = 1.5418 Å) operated at 40 kV, 30 mA and scanning speed 0.02°/s. Scanning electron microscopy (SEM) images were taken with a Hitachi S-4800 N scanning electron microscopy, using an accelerating voltage of 15 kV. Energy-dispersive X-ray (EDX) microanalysis of the samples was performed during SEM measurements. Transmission electron microscopy (TEM, JEOL, JEM-2010, operated at 200 kV) was also used to investigate the structures and morphology. UV-visible (UV–vis) spectra of the samples were measured on a UV–vis spectrophotometer (SHIMADZU-2550). Nitrogen adsorption/desorption tests at 77 K were conducted on a surface area and porosity analyzer (ASAP 2020 (V4.00H)). Fourier transform infrared spectroscopic (FT-IR) measurements were performed on PerkinElmer spectrometer (spectrum 100). The resolution was 4 cm^{-1} and KBr was used as background. X-ray photoelectron spectroscopy (XPS) measurement was performed on ESCALAB 250Xi electron spectrometer with Al Kα X-ray source. The photoluminescence (PL) spectrum was measured at room temperature with JASCO-FP6200 in a spectral range of 330–700 nm. A Xe lamp with a wavelength of 325 nm was used as the excitation source. The zeta potential was detected on Malvern Nano-ZS.

2.4. Measurement of photocatalytic activity

The photocatalytic activities of the as-obtained CeO_2 nanotube samples were evaluated by using photocatalytic removal of Cr(VI) at ambient temperature (20 °C) as probe reactions. Briefly, 50 mg as-prepared CeO_2 nanotubes were mixed with 60 mL 60–140 mg/L $K_2Cr_2O_7$ aqueous solution in a beaker with a volume of 100 mL, and then 0.05 g oxalic acid was added to keep an acidic medium. In a parallel experiment, 2 mL isopropanol was added into the mixture without the change of concentration of Cr(VI). Prior to illumination,
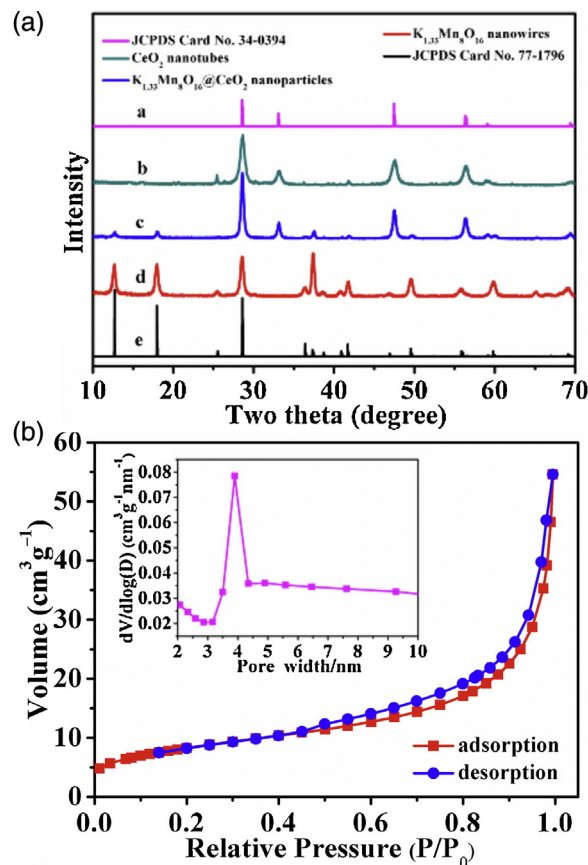
Fig. 1. (a) Typical powder XRD patterns of the obtained CeO_2 nanotubes (Curve b), nanowires (Curve c), and the starting $K_{1.33}Mn_8O_{16}$ nanowire precursor (Curve d). (b) Nitrogen sorption isotherms of CeO_2 nanotubes. The inset is the corresponding pore size distribution calculated from the desorption branch.

the suspension was sonicated before illumination for 30 s to obtain highly dispersed catalyst. After magnetic stirring in the dark for 1 h to establish the adsorption–desorption equilibrium, the beaker was placed under a commercial 500 W mercury lamp with an average light intensity of 37.6 μW cm^{-2}. At given time intervals 3 mL aliquot dispersions were sampled on constant stirring, followed by centrifugation to remove precipitates. The Cr(VI) reduction was determined colorimetrically at 540 nm using the diphenylcarbazide (DPC) method with a detection limit of 5 μg/L [34,35]. As a comparison, the photocatalytic reduction of Cr(VI) over P25 was also tested under the same conditions with 50 mg catalyst added. The photocatalytic performance was expressed by the I/I_0 vs t (min), where I_0 was the absorbance intensity of Cr(VI)-DPC complex of the initial concentration when adsorption–desorption equilibrium was achieved. I was the absorbance intensity of Cr(VI)–DPC complex at each irradiated time interval (10 min) of the main peak (540 nm). The reproducibility was checked by repeating the runs for five times. The interaction between oxalic acid/Cr(VI) and CeO$_2$ nanotube surface was examined by UV–vis absorption spectrum. CeO$_2$ nanotube suspensions (0.1 g/L) were prepared at room temperature with the addition of 0.05 g oxalic acid and/or 100 mg/L K$_2$Cr$_2$O$_7$ aqueous solution, and set for 12 h in the dark. The solid powder was collected by centrifugation (13,000 rpm) and then dried in dark at room temperature. Their UV–vis adsorption spectra were measured on a UV–vis spectrophotometer (SHIMADZU-2550) equipped with an integrating sphere attachment, using BaSO$_4$ as background.

3. Results and discussion

### 3.1. XRD and BET analysis of the samples

In our previous study, K$_{1.33}$Mn$_8$O$_{16}$ was found to have somewhat surprising chemical behavior in the aqueous solution of transition metal nitrates, which could be engaged in the reaction dynamic equilibrium of the hydrolysis of transition metal nitrates by consuming HNO$_3$ generated by the hydrolysis process. Continuing with this approach, the metastable K$_{1.33}$Mn$_8$O$_{16}$ nanowires were then treated in Ce(NO$_3$)$_3$ aqueous solution with or without the addition of SDBS, crystallizing CeO$_2$ nanotubes and heterostructured nanowires, respectively. Curve b in Fig. 1a shows the XRD pattern of CeO$_2$ nanotubes, which can be indexed to a cubic fluorite-structured cerium oxide with lattice parameters of $a = b = c = 5.411$ Å (JCPDS card no. 34-394). There occurs no variation in the diffraction pattern compared with standard one (Curve a, Fig. 1a). Two characteristic peaks from residual tetragonal phase K$_{1.33}$Mn$_8$O$_{16}$ nanowire precursor are also detected in this pattern ($2\theta = 25.52°$, 41.72°). The XRD data prove that K$_{1.33}$Mn$_8$O$_{16}$ nanowires are involved in the heterogeneous nucleation and crystallization of CeO$_2$ nanotubes in our designed chemical reaction system. Fig. 1b shows the textural characteristic of as-prepared CeO$_2$ nanotubes investigated by nitrogen adsorption–desorption measurement at 77 K. This isotherm profile shows a small hysteresis loop observed at a relative pressure of 0.4–1.0, indicating the presence of a mesoporous structure with BET surface area of 30.2 m^2/g. An irregular pore size distribution calculated from the desorption branch by the Barrett–Joyner–Halenda method (Inset of Fig. 1b) and centered at 3.9 nm is associated with the mesoporous structure of CeO$_2$ tubes. The structures provide communicable channels for chemical species traveling between the inner space of the hierarchically complex CeO$_2$ hollow architectures and the outer space of the solution phase environment, thus having intriguing wastewater treatment applications of adsorption and photocatalysis.

3.2. Morphology and structural studies of the samples

Fig. 2a includes a SEM image of the CeO$_2$ material obtained by hydrothermally treating K$_{1.33}$Mn$_8$O$_{16}$ nanowires in 0.1 M Ce(NO$_3$)$_3$ aqueous solution containing 0.1 g SDBS at 150–170 °C for 40–45 h.
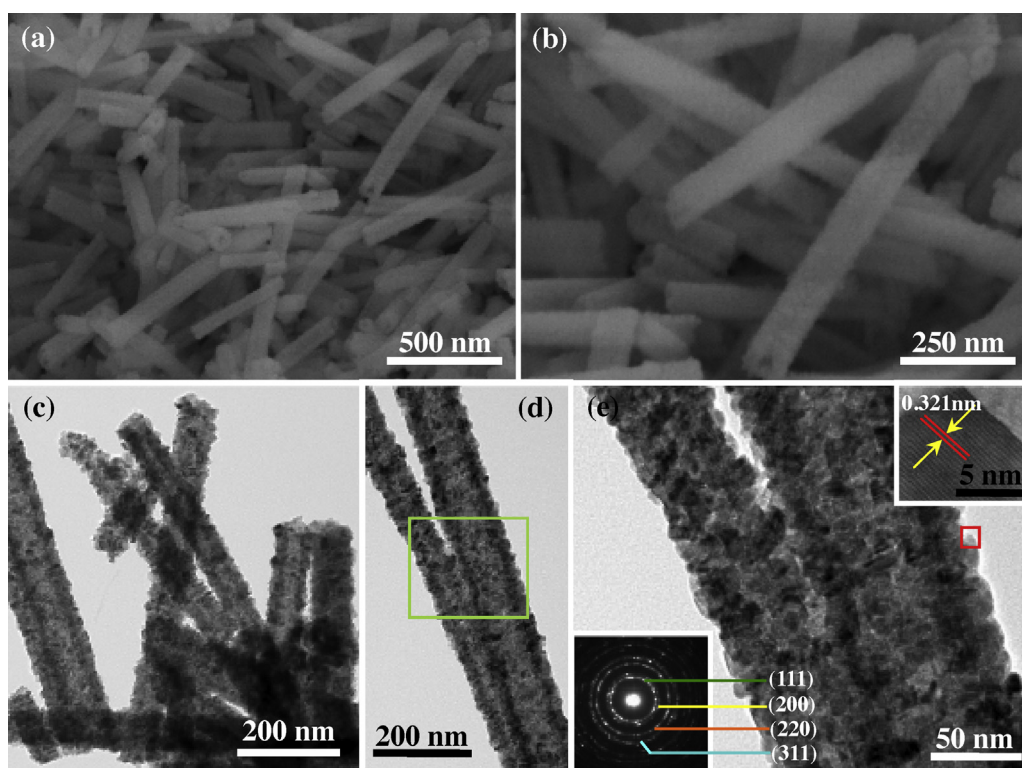
Fig. 2. Electron microscopy of representative CeO$_2$ nanotubes. (a and b) SEM images. (c and d) Low-magnification TEM images. (e) Corresponding high-magnification TEM image of selected area in (d). The insets of top right and bottom left are HRTEM image taken from the area marked with a red rectangle in (e), and SAED pattern of CeO$_2$ nanotubes, respectively.
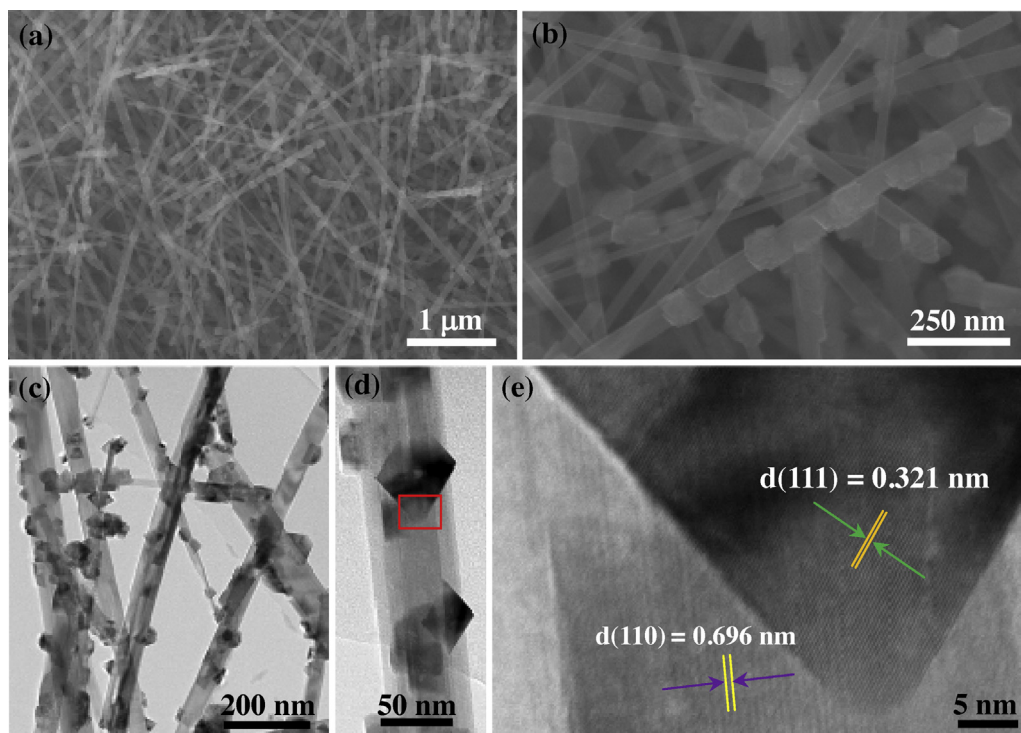
**Fig. 3.** Morphologies and crystal structures of CeO_2-decorated $K_{1.33}Mn_8O_{16}$ nanowires obtained by hydrothermally treating $K_{1.33}Mn_8O_{16}$ nanowires in 0.02 M $Ce(NO_3)_3$ aqueous solution without the addition of SDBS at 150–170 °C for 24 h. (a and b) SEM images of representative nanowires. (c) Low-magnification TEM image and (d) its magnified counterpart. (e) Lattice-resolved TEM image of nanowire marked in (d).

The procedure allows us to obtain tube-like nanostructures with a diameter of 90 ± 10 nm and a length of 0.6–1.2 μm. This diameter fits with those of $K_{1.33}Mn_8O_{16}$ nanowire templates. A high-magnification SEM image (Fig. 2b) further reveals that the surface of these nanotube is actually assembled from tiny nanoparticles. Some broken tubes show a porous nature of this type materials, which is confirmed by TEM observation in Fig. 2c–e. HRTEM image corresponding to fresh CeO_2 nanotubes is included in the top-right inset of Fig. 2e, illustrating clear lattice fringes of the region mapped from the red square (marked in Fig. 2e). The spacing of 0.321 nm between two adjacent lattice fringes corresponds to the $\{1\,1\,1\}$ crystal planes of CeO_2, which also confirms the high crystallinity and single-crystalline nature of these nanoscale building blocks. The well-defined diffraction spots exhibit four diffraction rings corresponding to $(1\,1\,1)$, $(2\,0\,0)$, $(2\,2\,0)$, and $(3\,1\,1)$ lattice planes, respectively (the bottom-left inset of Fig. 2e), which is consistent with typical XRD pattern (Curve b, Fig. 1a). The as-obtained CeO_2 hollow nanostructures are generated in situ via the assembly of randomly oriented CeO_2 nanocrystallites against the preexisting solid $K_{1.33}Mn_8O_{16}$ nanowires firstly. As shown in Fig. S1, $K_{1.33}Mn_8O_{16}$ nanowire core–CeO_2 shell structures can be obviously observed after hydrothermally treating $K_{1.33}Mn_8O_{16}$ nanowires for 5 h in 0.1 M $Ce(NO_3)_3$ aqueous solution containing 0.1 g SDBS at 150–170 °C, which agrees with the phenomenon of typical templating growth mechanism. The obtained core–shell structured intermediates are hydrothermally unstable in the existence of HNO_3 generated by the hydrolysis of $Ce(NO_3)_3$ in aqueous solution, and the dissolution of $K_{1.33}Mn_8O_{16}$ core results in the final formation of CeO_2 nanotubes.

To investigate the influence of the surfactant SDBS on the crystallization of CeO_2 nanotubes, experimentally, at a fixed concentration $Ce(NO_3)_3$ aqueous solution (0.1 M) while no SDBS was added, no CeO_2 nanotubes were crystallized after 35 h. A typical SEM image (Electronic Supplementary materials, Fig. S2A) reveals that this procedure leads to the growth of $K_{1.33}Mn_8O_{16}$ @ CeO_2

heterostructured nanowires and CeO_2 particles instead of CeO_2 nanotubes. After 45 h, no CeO_2 nanotubes were formed and long rod-like structures could be observed (Electronic Supplementary materials, Fig. S2B). Quick deposition process forms dense shell layer and makes the interface difficultly accessible for active HNO_3 species penetration, which restrains self-hollowing process. When the concentration of $Ce(NO_3)_3$ is further reduced to 0.02 M without the presence of SDBS, only $K_{1.33}Mn_8O_{16}$ @ CeO_2 heterostructured nanowires are generated, as shown in the XRD pattern (Curve c of Fig. 1a). Low concentration of $Ce(NO_3)_3$ decreases the deposition rate of CeO_2 nanocrystals on $K_{1.33}Mn_8O_{16}$ wires, and the resultant lower HNO_3 concentration cannot destroy $K_{1.33}Mn_8O_{16}$ wire-like structure. In this condition, heterogeneous nucleation of CeO_2 nanoparticles on $K_{1.33}Mn_8O_{16}$ wire surface dominates the growth of CeO_2. These CeO_2 nanocrystals clearly nucleate on $K_{1.33}Mn_8O_{16}$ wires as individual ones, as shown in Fig. 3a and b, which is a highly desired feature for materials requiring large surface areas, such as CeO_2-based catalysts. TEM images in Fig. 3c and d shows that the particles uniformly cover the surface of $K_{1.33}Mn_8O_{16}$ nanowires. The interface between nanowires and nanoparticles marked in the boxed region of Fig. 3d is further characterized by HRTEM (Fig. 3e), showing that $K_{1.33}Mn_8O_{16}$ nanowire is single crystal where the $\{1\,1\,0\}$ lattice fringes are well resolved and exhibit the correct spacing of 0.696 nm. The attached CeO_2 nanoparticles are also highly crystalline with measured interplanar d-spacing of around 0.321 nm fitting well to CeO_2 $\{1\,1\,1\}$ planes. The efficient decoration of CeO_2 particles on $K_{1.33}Mn_8O_{16}$ materials suggests a promising strategy for engineering crystal surface on the basis of heterogeneous crystallization. These results also indicate that the presence of the surfactant SDBS is essential to regulate the hollowing growth process of the CeO_2 nanotubes.

It is evident from many studies that soluble surfactant molecules present in the growth medium adhere to the surfaces of growing crystals and influence crystal growth [36]. A more interesting prospective application of surface selective surfactants would be to
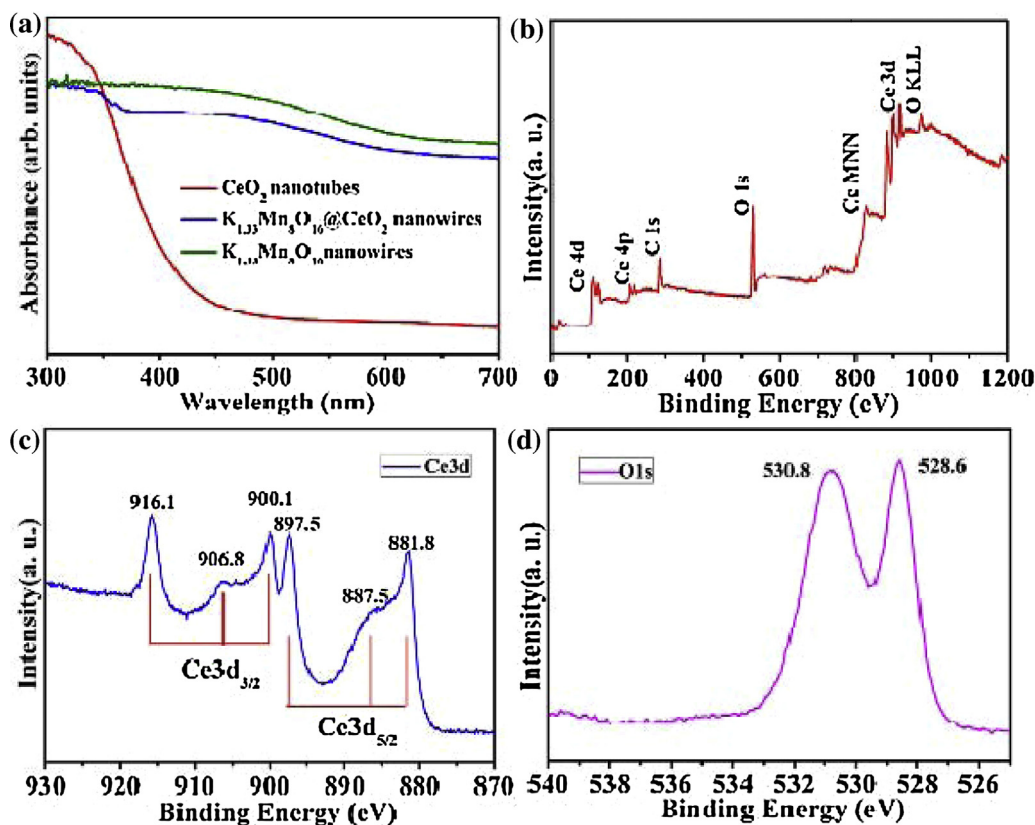
Fig. 4. (a) UV–vis absorption spectra of $K_{1.33}Mn_8O_{16}$ nanowire precursor, as-obtained nanowires, and CeO_2 nanotubes. (b) Full-range XPS spectrum of CeO_2 nanotubes. (c) XPS spectrum of Ce 3d. (d) XPS spectrum of O 1s.

finely tune the surface crystallization on existing solid faces to follow the resulting shape evolution process. We address this issue by presenting the study of the shape evolution process via surface crystallization control in the kinetic growth regime of CeO_2 nanotubes. Anionic surfactant SDBS has a unique parent structure with hydrophilic groups and lipophilic groups, and can bind to $K_{1.33}Mn_8O_{16}$ nanowire surface [37], preventing the potentials for the swift heterogeneous nucleation of CeO_2 nanoparticles on the surface. Chemical reactions between $K_{1.33}Mn_8O_{16}$ precursor and HNO_3 induce the generation of active surface sites for the opening up of new heteronucleation and the subsequent CeO_2 crystallization against the pre-existing solid precursor. The zeta potential values of $K_{1.33}Mn_8O_{16}$ nanowires in SDBS aqueous solution and $Ce(NO_3)_3$ aqueous solutions are -38.8 mV and 28.5 mV, respectively, indicating that anionic SDBS surfactant molecules can be adsorbed on $K_{1.33}Mn_8O_{16}$ nanowires via electrostatic interaction in $Ce(NO_3)_3$ aqueous solution. The adsorption binding of SDBS molecules to $K_{1.33}Mn_8O_{16}$ nanowire, and the crystallization of CeO_2 by the hydrolysis process of $Ce(NO_3)_3$ on nanowire are two concurrent and compete processes occurred in aqueous solution. Tuning synergistic effects of the two process can change the heterogeneous crystallization rate of CeO_2 on solid surface of $K_{1.33}Mn_8O_{16}$ nanowire, and thus can enable CeO_2 growth process to proceed at an appreciable rate to coat $K_{1.33}Mn_8O_{16}$ nanowire. It is observed that the concentration of SDBS is important during the crystallization of CeO_2 nanotubes. The surfactant molecules at a higher concentration are considered to form densely coated $K_{1.33}Mn_8O_{16}$ nanowires by SDBS molecules, preventing the heterogeneous nucleation to create new hybrid materials in organic-inorganic interface (Electronic Supplementary materials, Fig. S3). It is found that 0.1 g SDBS is the optical quantity for the hydrothermal growth of CeO_2 nanotubes in 0.1 M $Ce(NO_3)_3$

aqueous solution at 150–170 °C. The SDBS surfactant molecules are able to exchange on and off the growing crystals, so that nanoscale regions of $K_{1.33}Mn_8O_{16}$ nanowire surface are transiently accessible for heterogeneous nucleation and growth of CeO_2 nanoparticles, yet entire crystals are still wire-like structures with CeO_2 shell and $K_{1.33}Mn_8O_{16}$ core. Typically, this process is characterized by kinetically favored initial deposition of CeO_2 nanoparticles on $K_{1.33}Mn_8O_{16}$ template owing to the hydrolysis of $Ce(NO_3)_3$ in aqueous solution. However, the resultant $K_{1.33}Mn_8O_{16}/CeO_2$ core/shell structured nanowires (Electronic Supplementary materials, Fig. S1) remain out of equilibrium with the surrounding solution due to higher solubility of $K_{1.33}Mn_8O_{16}$ template in the presence of HNO_3 derived from the hydrolysis of $Ce(NO_3)_3$, and thus the $K_{1.33}Mn_8O_{16}$ core dissolves and becomes progressively depleted to produce intact hollow CeO_2 nanostructure via a templating process.

3.3. Optical properties and composition analysis of the samples

Fig. 4a shows room temperature UV–vis absorption spectra of the as-prepared samples. As can be observed, the wavelength of the absorption edges, calculated for convenience by extrapolation of a linear part of the absorption rise, is 426 nm for CeO_2 nanotubes, corresponding to a band gap energy of 2.9 eV. In the case of the heterostructured nanowires, except for the characteristic absorption band edge of CeO_2 in UV light range, a feature band edge of pure $K_{1.33}Mn_8O_{16}$ appears in the visible region based on its UV–vis spectrum, thus confirming that CeO_2 nanoparticles have been anchored successfully on the surface of $K_{1.33}Mn_8O_{16}$ nanowires. The prepared CeO_2 nanotubes were investigated by XPS to study the surface compositions. As seen in Fig. 4b, the peaks of Ce3d and O1s can be identified, and no peaks ascribable to heteroelements are observed except the C1s peak that originates from

contaminated carbon of specimens. The high-resolution Ce3d XPS spectrum shows six peaks at binding energy of 881.8, 887.5, 897.5, 900.1, 906.8, and 916.1 eV, which are in good agreement with that of the pure CeO_2 [38]. The peaks at around 881.8, 887.5 and 897.5 eV are assigned to Ce3$d_{5/2}$, and the peaks at around 900.1, 906.8, and 916.1 eV are assigned to Ce3$d_{3/2}$. The spectrum also shows the presence of a mixed valence state (Ce^{3+} and Ce^{4+}) for the synthesized CeO_2 nanotubes (Fig. 4c), demonstrating the presence of oxygen vacancy centers in the CeO_2 crystal lattice. The O1s peak centered at 528.6 eV (Fig. 4d) is ascribable to the O^{2-} bound to the cerium in the lattice; whereas, the presence of a peak at 530.8 eV corresponds to the surface hydroxidic species and/or ambient moisture [39].

3.4. UV-light driven photoreduction of Cr(VI) in aqueous solution

3.4.1. Effect of small molecular weight organics on photoreduction of Cr(VI)

The prepared CeO_2 materials can be applied in photocatalytic removal of heavy metal Cr(VI) ions. One practical problem in photoreduction of Cr(VI) using semiconductors is the undesirable electron/hole recombination which presents the major energy-wasting step thus limiting the achievable quantum yield without proper electron acceptor or donor. An addition of small molecular weight organics significantly accelerates the photoreduction of Cr(VI) in the presence of CeO_2 nanotubes. Isopropanol is the simplest secondary alcohol, which has been widely used in photocatalysis process in order to accelerate photochemical reactions [40]. When 2 mL isopropanol was added into 60 mL 100 mg/L $K_2Cr_2O_7$ aqueous solution over 50 mg CeO_2 nanotubes, an acceleration of Cr(VI) photoreduction was observed in the heterogeneous systems and 78.9% of initial Cr(VI) was removed after 60 min UV light irradiation (Fig. 5a and b). The results suggest that the photocatalyst-driven reduction of Cr(VI) is mainly facilitated by photoexcited electrons, and thus better electron–hole separation is achieved in this reduction process where small molecular weight isopropanol is added.

Other than small molecular weight alcohol, we found that the addition of appropriate small molecular weight organic acid, e.g., oxalic acid, better triggered the photoreduction of Cr(VI) over CeO_2 nanotubes. Oxalic acid is a simple model organic compound with two carboxyl groups, and its behavior during heterogeneous photocatalytic process is representative for some of the main features of the whole class of small molecular weight organic acids. Oxalic acid can be easily oxidized to CO_2, thus minimizing the problem of possible accumulation of undesirable intermediate chemical products [41]. Fig. 6a shows time-dependent UV–vis absorption spectral pattern of DPC–Cr(VI) complex solution after the reduction of 60 mL 100 mg/L $K_2Cr_2O_7$ aqueous solution over 50 mg CeO_2 nanotubes in the presence of 0.05 g oxalic acid. After UV light irradiation for 50 min, the conversion reaches 99.6% for Cr(VI) over CeO_2 nanotubes (the inset of Fig. 7a), showing a superior photocatalytic performance compared with isopropanol additive by which 64.3% of Cr(VI) is reduced after the same period of time. The experiment was conducted using CeO_2 nanotubes directly in the absence of oxalic acid under UV light irradiation. Slight variation was observed in the concentration of Cr(VI) (Fig. 6b). Because CeO_2 bandgap is usually attributed to an $O2p \rightarrow Ce4f$ transition, CeO_2 is not generally regarded as a photoactive material. Unexpectedly, the UV light photocatalytic reduction of Cr(VI) over CeO_2 is promoted by oxalic acid. Again blank test was also carried out without the addition of the CeO_2 catalyst under UV light exposure, and there occurs small change of Cr(VI) concentration in the presence of 0.05 g oxalic acid, as displayed in Fig. 6b. It indicates that the direct redox reactions between Cr(VI) and oxalic acid are weak, and do not dominate the chemical removal process of Cr(VI) in the simulated wastewater. Importantly, as compared with 50 mg
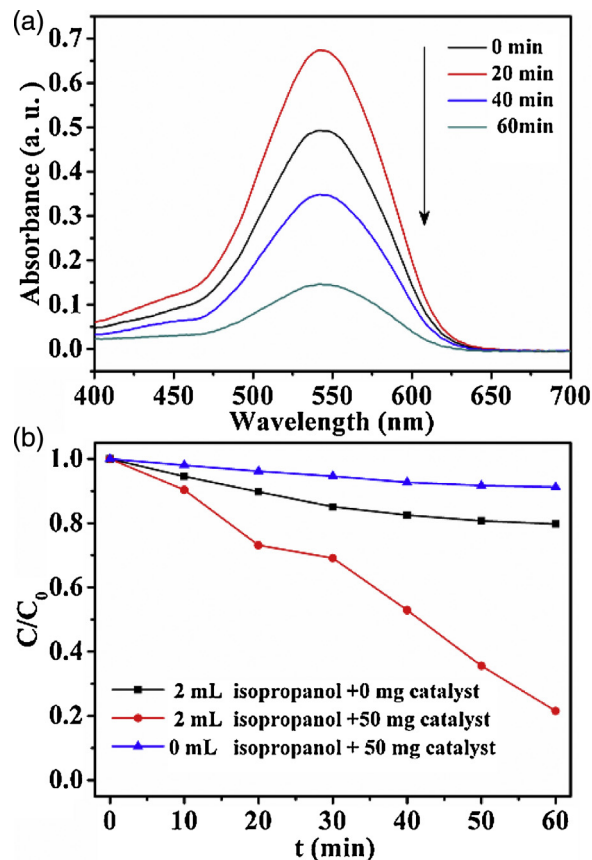
Fig. 5. (a) Time-dependent absorption spectral pattern of DPC–Cr(VI) complex solutions after the reduction of 60 mL 100 mg/L $K_2Cr_2O_7$ aqueous solution over 50 mg CeO_2 nanotubes in the presence of 2 mL isopropanol. (b) A comparison on photocatalytic reduction of 60 mL 100 mg/L $K_2Cr_2O_7$ aqueous solution over 50 mg as-prepared samples under UV light irradiation with the addition of 2 mL isopropanol.

commercial P25-TiO$_2$ powder, 85.6% Cr(VI) is removed under UV light irradiation for 50 min in 60 mL 100 mg/L $K_2Cr_2O_7$ aqueous solution containing 0.05 g oxalic acid (Fig. 6b). Although the removal rate of Cr(VI) on CeO_2 nanotubes is not improved greatly compared with that of P25 powder, we believe that our work provides a new approach to realize high efficiency photocatalytic removal of toxic Cr(VI) from water. Note further that the reduction rate decreases with the increase of Cr(VI) concentration from 60 to 100 mg/L, and a further increase in the concentration of Cr(VI) to 140 mg/L leads to a rapid decrease in the removal efficiency, as shown in Fig. 7a, strongly indicating that as-obtained CeO_2 nanotubes facilitate photocatalytic reduction removal of Cr(VI) with concentration under 100 mg/L. The obtained kinetic data of the Cr(VI) reduction reaction over CeO_2 nanotubes can be fitted to a pseudo-first-order model as expressed by $\ln(C_0/C) = kt$, where C_0 and C represent the Cr(VI) concentration before and after the UV light irradiation, t is the irradiation time, and k is the apparent rate constant. As shown in Fig. 7b, the plots $\ln(C_0/C)$ versus t for the concentrations 60 mg/L, 100 mg/L, and 140 mg/L describe a linear behavior. The apparent rate constant k of Cr(VI) reduction reaction is about 0.10294 min^{-1} for the concentration 60 mg/L, which is more than 7.77 times higher than that for concentration 140 mg/L (0.01324 min^{-1}). The results also indicate that as-obtained CeO_2 nanotubes should be a novel ideal UV light-responsive photocatalyst for Cr(VI) removal in aqueous solution.
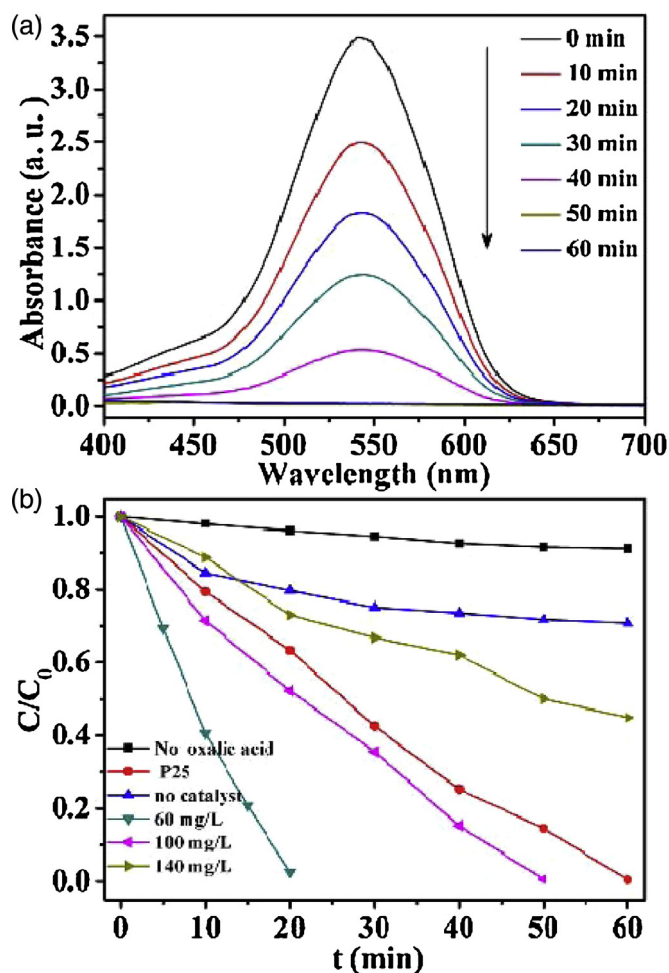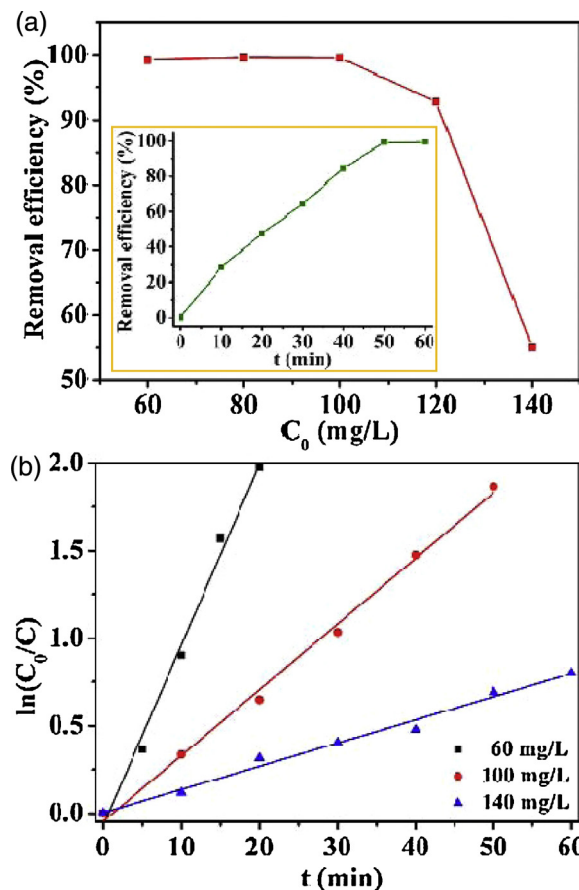
Fig. 6. The photoreduction of 60 mL 100 mg/L $K_2Cr_2O_7$ aqueous solution over 50 mg CeO_2 nanotubes with the assistance of 0.05 g oxalic acid. (a) Time-dependent absorption spectra of DPC–Cr(VI) complex. (b) A comparison study of photocatalytic performance in the presence of 0.05 g oxalic acid, together with the results from the blank experiments with UV light irradiation (0 g CeO_2 nanotube catalyst but 0.05 g oxalic acid, or no oxalic acid but 50 mg CeO_2 nanotubes).

Fig. 7. (a) The removal efficiency of Cr(VI) under 60 min UV light irradiation for 60 mL $K_2Cr_2O_7$ aqueous solution with different concentrations over 50 mg CeO_2 nanotubes in the presence of 0.05 g oxalic acid. The inset indicates the change of the removal efficiency with UV light irradiation time in 60 mL 100 mg/L $K_2Cr_2O_7$ aqueous solution over 50 mg CeO_2 nanotubes (oxalic acid: 0.05 g). (b) Kinetics of photoreduction of Cr(VI) for different concentrations of $K_2Cr_2O_7$ aqueous solution.

3.4.2. Structure and composition analysis of CeO_2 nanotubes after reaction

To confirm the UV-light photoreduction of Cr(VI) to Cr(III), XPS measurement was carried out to investigate chemical states of cerium and chromium on CeO_2 nanotubes before and after photocatalysis reactions (the photoreduction was in 60 mL 100 mg/L $K_2Cr_2O_7$ aqueous solution over 50 mg CeO_2 nanotubes with the assistance of 0.05 g oxalic acid). There are no changes of the survey XPS and Ce3d XPS spectra of the sample before and after reaction (Fig. 8a and b), indicating the good chemical stability of the sample in the photochemical reaction process. In the narrow scan spectrum of the Cr2p there are not peaks of Cr(III) signal on CeO_2 nanotubes before photoreduction reaction (Fig. S4), and only weak Cr(VI) signal around 580 eV is observed suggesting that Cr(VI) species could hardly be adsorbed on the surface of CeO_2 nanotubes in the solution. However, more chromium signals occur after photoreactions. As shown in Fig. 8c, the Cr2p peaks can be curve-fitted with three components at binding energy of 576.8, 581.8 and 586.8 eV, assigned to Cr(III) $2p_{3/2}$, Cr(VI) $2p_{3/2}$, and Cr(III) $2p_{1/2}$, respective [42,43]. The result indicates that Cr(III) species are the dominant existing form on the surface of CeO_2 nanotubes after photocatalysis reactions, and confirms the photoreduction of Cr(VI) occurred under the UV light illumination.

It has been reported that surface defects are important adsorption sites and active sites for heterogeneous photocatalysis, which are presumed to affect the electron–hole recombination process and to create a broad distribution of surface electronic states mediating the exchange of electrons between the surface of photocatalyst and the adsorbed reacting species [44]. Fig. S5 in the Electronic Supplementary materials shows the PL spectrum of the as-obtained CeO_2 nanotubes at an excitation wavelength of 325 nm. The emission peak located approximately at 370 nm is attributed to an intense 4f–5d transition of Ce^{3+} in cerium compounds [45], thus further confirming the presence of Ce^{3+} ions in the synthesized CeO_2 nanotubes. The two weak visible peaks at λ = 450 and 465 nm corresponds to defect emissions. The surface defect site concentration is thus relatively low due to the weak PL emission peaks in visible light region, leading to a low rate of photocatalytic activity of as-prepared CeO_2 nanotubes without the addition of oxalic acid. According to comparative experiments under the same conditions and procedures mentioned above, the photocatalytic decontamination of Cr(VI) using CeO_2 nanotubes or oxalic acid alone under UV light irradiation is slow. However, the photoreduction of Cr(VI) by CeO_2 nanotubes is markedly improved when oxalic acid is added into the reaction system, confirming a highly significant synergistic effect in the photocatalytic decontamination of Cr(VI) with CeO_2 nanotubes as the photocatalyst. Above results also suggest that the synergistic effect is dependent of the structure of small molecular weight organic additives. It is the carboxylic groups of additives rather than hydroxyl groups that determine the
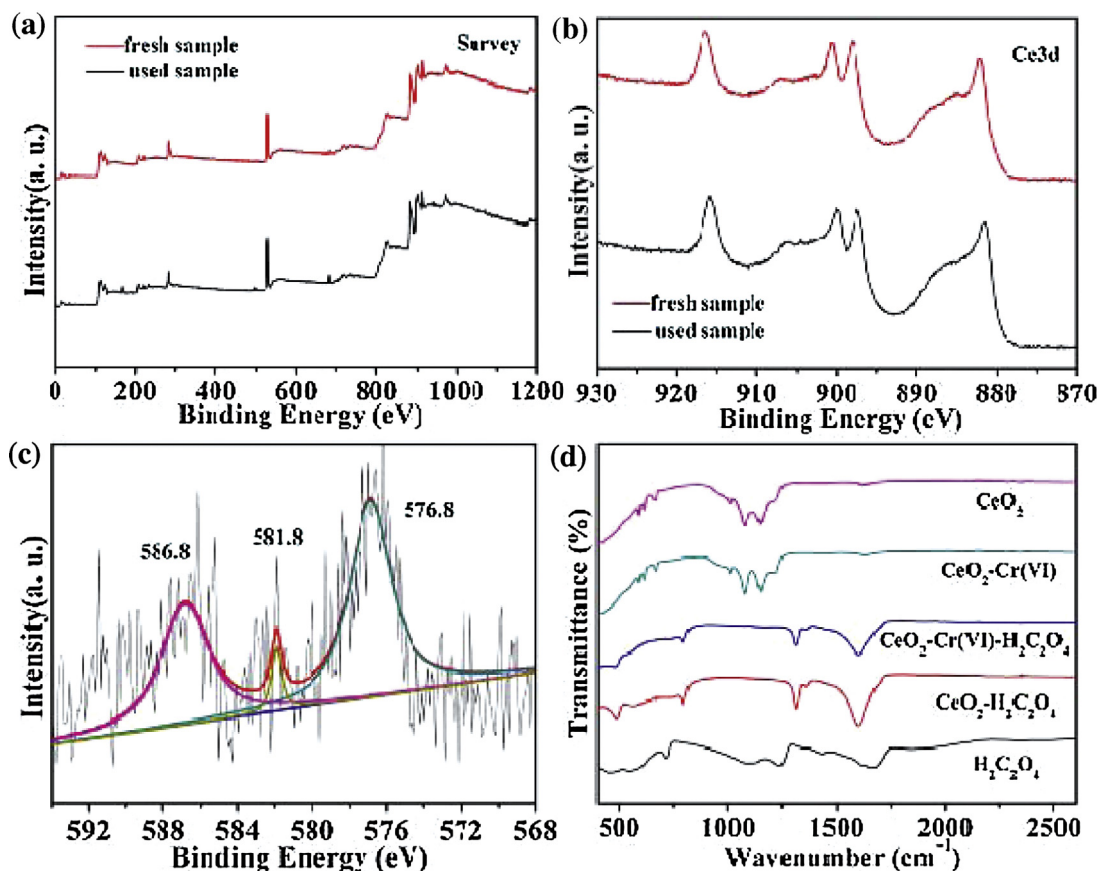
Fig. 8. (a) XPS survey spectra and (b) Ce3d XPS spectra of prepared CeO$_2$ nanotube before and after photocatalytic reduction (the photoreduction was in 60 mL 100 mg/L K$_2$Cr$_2$O$_7$ aqueous solution over 50 mg CeO$_2$ nanotubes with the assistance of 0.05 g oxalic acid). (c) High-resolution Cr2p XPS spectrum of chromium on CeO$_2$ nanotube after photoreaction. (d) FTIR spectra of CeO$_2$ nanotubes before and after oxalic acid and/or Cr(VI) adsorption, confirming the interaction between oxalic acid and CeO$_2$ nanotube surface. No interaction between Cr(VI) and CeO$_2$ nanotube surface was observed.

kinetics for CeO$_2$ photocatalytic reduction of Cr(VI). Many organic compounds with carboxylic groups are able to make charge transfer complex between oxides and the surface adsorbents via a fairly strong interaction [46]. It has been reported that the dicarboxylic oxalic acid may strongly bind on oxide surface via ester linkages or in a bidentate chelate fashion [47,48]. As shown in Fig. 8d, no changes are observed in the FTIR spectra between CeO$_2$ and CeO$_2$–Cr(VI). However, FTIR spectra of CeO$_2$ nanotubes before and after oxalic acid adsorption show new absorption peaks compared with that of pure oxalic acid, confirming the interaction between oxalic acid and CeO$_2$ nanotube surface. From the UV–vis absorption spectra in Fig. 9a, one can see that the absorption spectrum of the mixture of oxalic acid and Cr(VI) solution is proximately equal to

the sum of their individual spectra, also indicating no observable interaction between Cr(VI) and the oxalic acid molecules. The weak visible light absorption and two strong characteristic UV absorption bands of Cr(VI) result in significant increase of the absorption edge of Cr(VI)-adsorbed CeO$_2$ nanotubes compared with pure CeO$_2$ nanotubes, as shown in Fig. 9b. However, once oxalic acid molecules are adsorbed on CeO$_2$ surface, the absorption spectrum of CeO$_2$ is blue shifted from 430 nm to 400 nm (Fig. 9b). It implies a surface complex is formed on oxalic acid-adsorbed CeO$_2$ nanotube and may be attributed to the ligand-to-metal charge–transfer transition within the surface complexes [41,49,50]. The coexistence of Cr(VI) significantly increases the absorption intensity in UV light region of the ternary CeO$_2$–oxalic acid–Cr(VI) system (Fig. 9b),
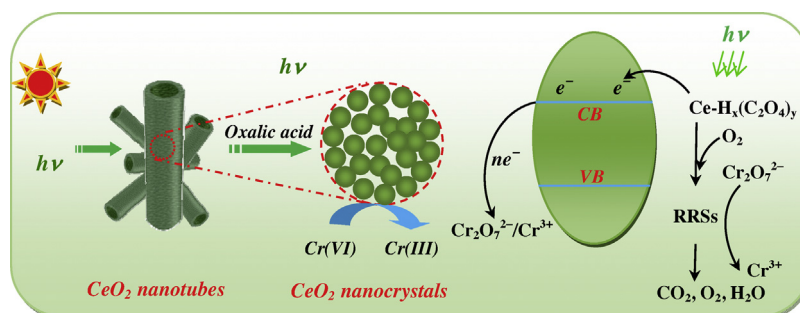
Scheme 1. Schematic illustration of the mechanism of the oxalic acid-induced photocatalytic reduction of Cr(VI) by CeO$_2$ nanotubes under UV light irradiation. RRSs represent reactive reductive species.

Fig. 10. Effect of (a) $H_2C_2O_4$ and (b) NaF on the photocatalytic reduction of Cr(VI) under 60 min UV light irradiation for 60 mL 100 mg/L $K_2Cr_2O_7$ aqueous solution over 50 mg CeO_2 nanotubes.
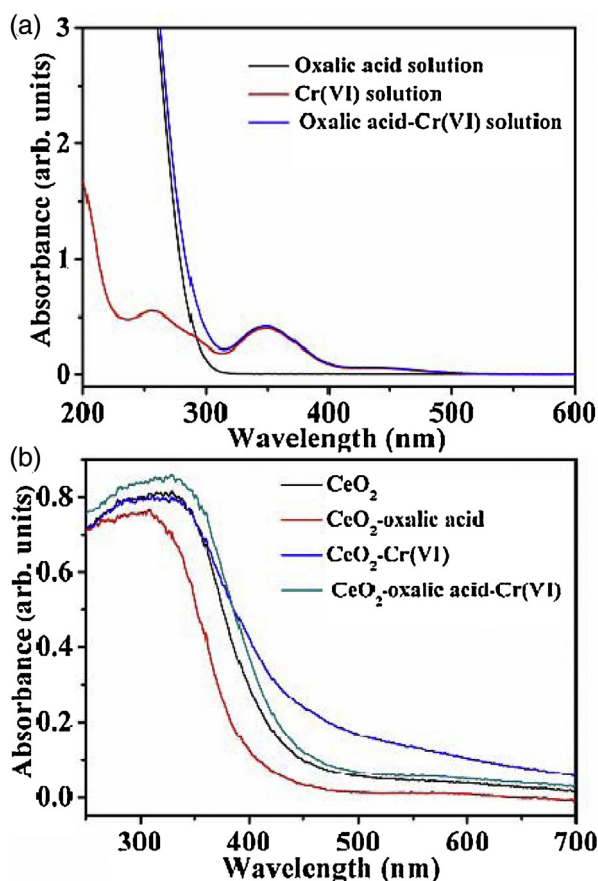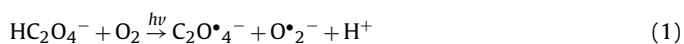
Fig. 9. UV–vis absorption spectra of (a) the solution-phase systems composed of oxalic acid, Cr(VI), and oxalic acid–Cr(VI), and (b) the solid-phase system composed of CeO_2, CeO_2–oxalic acid, CeO_2–Cr(VI), and CeO_2–oxalic acid–Cr(VI).
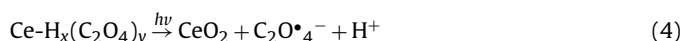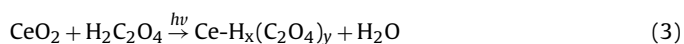
thus improving the UV-light photocatalytic activity of Cr(VI) reduction.

3.4.3. The mechanism of synergistic photocatalytic removal of Cr(VI)

In view of the observation obtained in this study, a possible mechanism of photocatalytic reduction of Cr(VI) by oxalic acid over CeO_2 nanotubes is proposed. As shown in Scheme 1, the photo-catalytic performance of CeO_2 nanotubes is improved due to the presence of light scattering in hierarchically structured nanocrystal aggregates, by which the traveling distance of UV light within the disordered structure is significantly extended, thus increasing the opportunities for incident photons to be captured by the designed CeO_2–oxalic acid system. Considering that oxalic acid alone could cause a slow photoreduction of Cr(VI) (Fig. 6b), organic radicals are generated owing to the absorption of UV light by oxalic acid molecules [41,51–56].

$$HC_2O_4^- + O_2 \xrightarrow{h\nu} C_2O^\bullet{}_4^- + O^\bullet{}_2^- + H^+ \tag{1}$$

$$C_2O^\bullet{}_4^- \xrightarrow{h\nu} CO^\bullet{}_2^- + CO_2 \tag{2}$$

The added oxalic acid interacted with CeO_2 to form CeO_2–oxalic acid surface complex.

$$CeO_2 + H_2C_2O_4 \xrightarrow{h\nu} Ce\text{-}H_x(C_2O_4)_y + H_2O \tag{3}$$

$$Ce\text{-}H_x(C_2O_4)_y \xrightarrow{h\nu} CeO_2 + C_2O^\bullet{}_4^- + H^+ \tag{4}$$

The illumination of UV light initiates the CeO_2–oxalic acid complex with high photochemical activity to generate organic radicals

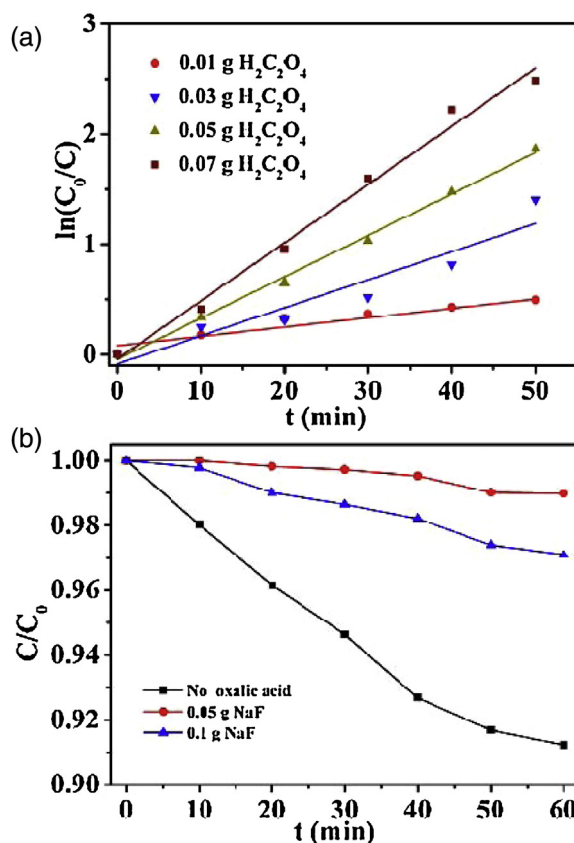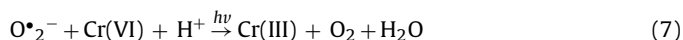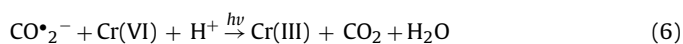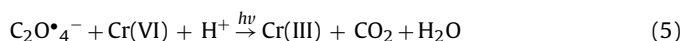such as $C_2O^\bullet{}_4^-$ from surface adsorbed oxalic acid through a ligand-to-metal charge–transfer pathway, resulting in the photoreduction of Cr(VI). The main reactions mentioned above are summarized as follows:

$$C_2O^\bullet{}_4^- + Cr(VI) + H^+ \xrightarrow{h\nu} Cr(III) + CO_2 + H_2O \tag{5}$$

$$CO^\bullet{}_2^- + Cr(VI) + H^+ \xrightarrow{h\nu} Cr(III) + CO_2 + H_2O \tag{6}$$

$$O^\bullet{}_2^- + Cr(VI) + H^+ \xrightarrow{h\nu} Cr(III) + O_2 + H_2O \tag{7}$$

The generation of CO_2 was confirmed by a designed experiment [57], as shown in Fig. S6 in the Electronic Supplementary materials. The photocatalytic reduction of Cr(VI)–Cr(III) consumes protons in acidic solution, which is thus dependent on pH values according to the proposed reaction process. Thereby, the reduction of Cr(VI)–Cr(III) is enhanced at acidic condition, and it is reasonable that the reduction of Cr(VI)–Cr(III) increases with oxalic acid concentration. From the pseudo-first-order reaction data shown in Fig. 10a, it can be seen that the photocatalytic reduction of Cr(VI) is significantly enhanced with the addition amount of oxalic acid (Electronic Supplementary materials, Table S1). The UV light irradiation induces the intramolecular electron transfer from oxalic acid ligand to Ce metal moiety, leading to the formation of organic radicals which react with Cr(VI) to produce Cr(III). Thus the Ce-$H_x(C_2O_4)_y$ surface complex formation is of primary importance for the UV light activation. NaF favors the formation of a complex with oxides by replacing surface hydroxyl groups [58]. It can be observed that the photocatalytic reduction of Cr(VI) is obviously depressed owing to the surface replacement of $^-$OH by F$^-$ (Fig. 10b), further confirming the interaction between surface hydroxyl groups of CeO_2 nanotubes and carboxylic groups of oxalic acid,

which is responsible for the improvement of photocatalytic activity in the presence of oxalic acid in Cr(VI) aqueous solution containing CeO$_2$ nanotube catalyst. Fig. S7 in the Electronic Supplementary materials shows performance of the recycled CeO$_2$ nanotubes for the photoreduction of Cr(VI) (50 min of UV light irradiation for each cycle). The recycled CeO$_2$ nanotubes were separated by centrifugation and reused without other treatments. It is found that the Cr(VI) removal efficiency is still up to 98.8% after five cycles, demonstrating a feasibility of recovery and reuse of CeO$_2$ nanotubes.

5. Conclusions

Morphology-tunable synthesis of CeO$_2$-based nanostructures is achieved by our proposed nanowire-directed templating method via fine-tuning K$_{1.33}$Mn$_8$O$_{16}$ nanowire surface chemistry in hydrothermal conditions. We note changes in the morphology of CeO$_2$ nanotubes and the decorative growth of solid CeO$_2$ particles on K$_{1.33}$Mn$_8$O$_{16}$ nanowires with the variation of the concentration of surfactant SDBS. When used as photocatalyst with the assistance of oxalic acid, the obtained CeO$_2$ nanotubes possess enhanced ability for Cr(VI) photoreduction at room temperature. A possible rationalization is that the small molecular weight organic acid is beneficial to the CeO$_2$ surface complex formation which induces the intramolecular electron transfer from oxalic acid ligand to Ce metal moiety under UV light irradiation based on a ligand-to-metal charge–transfer transition mechanism within the surface complexes, thus resulting in the high Cr(VI) reducing ability of the designed solid–liquid two-phase system. Because of the non-toxicity of oxalic acid additive and operation simplicity, our work provides an alternative way for the efficient photocatalysis reduction of Cr(VI), thus showing great promise for a wide range of challenging Cr(VI) separations in environmental water protection.

Acknowledgments

Appendix A. Supplementary data

Supplementary data associated with this article can be found, in the online version, at http://dx.doi.org/10.1016/j.apcatb.2015.03.040.

References

[1] A. Angell, Nat. Mater. 11 (2012) 362–364.
[2] G. Crini, Bioresour. Technol. 97 (2006) 1061–1085.
[3] C.E. Barrera-Diaz, V. Lugo-Lugo, B. Bilyeu, J. Hazard. Mater. 223–224 (2012) 1–12.
[4] M.A. Shannon, P.W. Bohn, M. Elimelech, J.G. Georgiadis, B.J. Marinas, A.M. Mayes, Nature 452 (2008) 301–310.
[5] J. Fei, J. Li, Adv. Mater. 27 (2015) 314–319.
[6] C.W. Abney, J.C. Gilhula, K. Lu, W. Lin, Adv. Mater. 26 (2014) 7993–7997.
[7] H. Tong, S. Ouyang, Y. Bi, N. Umezawa, M. Oshikiri, J. Ye, Adv. Mater. 24 (2012) 229–251.
[8] Y. Sang, Z. Zhao, M. Zhao, P. Hao, Y. Leng, H. Liu, Adv. Mater. 27 (2015) 363–369.
[9] D.M. Chen, Z.H. Wang, T.Z. Ren, H. Ding, W.Q. Yao, R.L. Zong, Y.F. Zhu, J. Phys. Chem. C 118 (2014) 15300–15307.
[10] Y. Li, Y. Liu, J. Wang, E. Uchaker, Q. Zhang, S. Sun, Y. Huang, J. Lic, G. Cao, J. Mater. Chem. A 1 (2013) 7949–7956.
[11] J. Wu, J. Wang, H. Li, Y. Du, X. Jia, B. Liu, CrystEngComm 16 (2014) 9675–9684.
[12] Y.F. Liu, W.Q. Yao, D. Liu, R.L. Zong, M. Zhang, X.G. Ma, Y.F. Zhu, Appl. Catal. B: Environ. 163 (2015) 547–553.
[13] J. Ran, J. Zhang, J. Yu, M. Jaroniec, S. Qiao, Chem. Soc. Rev. 43 (2014) 7787–7812.
[14] M. Kebir, M. Chabani, N. Nasrallah, A. Bensmaili, M. Trari, Desalination 270 (2011) 166–173.
[15] M.A. Gondal, M.A. Dastageer, S.G. Rashid, S.M. Zubair, M.A. Ali, D.H. Anjum, J.H. Lienhard, G.H. McKinley, K. Varanasi, Sci. Adv. Mater. 5 (2013) 2007–2014.
[16] E. Hu, X. Gao, A. Etogo, Y. Xie, Y. Zhong, Y. Hu, J. Alloys Compd. 611 (2014) 335–340.
[17] L. Yang, W. Sun, S. Luo, Y. Luo, Appl. Catal. B: Environ. 156–157 (2014) 25–34.
[18] Q. Wu, J. Zhao, G. Qin, C. Wang, X. Tong, S. Xue, Appl. Catal. B: Environ. 142–143 (2013) 142–148.
[19] S.J. Tesh, T.B. Scott, Adv. Mater. 26 (2014) 6056–6068.
[20] Y.C. Zhang, M. Yang, G. Zhang, D.D. Dionysiou, Appl. Catal. B: Environ. 142–143 (2013) 249–258.
[21] Y. Yang, G. Wang, Q. Deng, D.H.L. Ng, H. Zhao, ACS Appl. Mater. Interfaces 6 (2014) 3008–3015.
[22] X. Hua, H. Jia, F. Chang, Y. Luo, Catal. Today 224 (2014) 34–40.
[23] H. Ma, J. Shen, M. Shi, X. Lu, Z. Li, Y. Long, N. Li, M. Ye, Appl. Catal. B: Environ. 121–122 (2012) 198–205.
[24] X. Yin, W. Liu, J. Ni, Chem. Eng. J. 248 (2014) 89–97.
[25] Z. Yang, J. Wei, H. Yang, L. Liu, H. Liang, Y. Yang, Eur. J. Inorg. Chem. 10 (2010) 3354–3359.
[26] J. Wei, Z. Yang, Y. Yang, CrystEngComm 13 (2011) 2418–2424.
[27] Z.R. Tang, Z. Zhang, Y.J. Xu, RSC Adv. 1 (2011) 1772–1777.
[28] X.J. Lang, X.D. Chen, J.C. Zhao, Chem. Soc. Rev. 43 (2014) 473–486.
[29] S. Lin, G. Su, M. Zheng, D. Ji, M. Jia, Y. Liu, Appl. Catal. B: Environ. 123–124 (2012) 440–447.
[30] H. Bao, Z. Zhang, Q. Hua, W. Huang, Langmuir 30 (2014) 6427–6436.
[31] M.M. Khan, S.A. Ansari, M.O. Ansari, B.K. Min, J. Lee, M.H. Cho, J. Phys. Chem. C 118 (2014) 9477–9484.
[32] Q. Dai, J. Wang, J. Yu, J. Chen, J. Chen, Appl. Catal. B: Environ. 144 (2014) 686–693.
[33] J. Wu, H. Li, J. Wang, Z. Li, J. Nanosci. Nanotechnol. 13 (2013) 5452–5460.
[34] Y.C. Zhang, L. Yao, G. Zhang, D.D. Dionysiou, J. Li, X. Du, Appl. Catal. B: Environ. 144 (2014) 730–738.
[35] D. Shao, X. Wang, Q. Fan, Micropor. Mesopor. Mater. 117 (2009) 243–248.
[36] Y. Yin, A.P. Alivisatos, Nature 437 (2005) 664–670.
[37] J. Wu, J. Wang, H. Li, Y. Du, K. Huang, B. Liu, J. Mater. Chem. A 1 (2013) 9837–9847.
[38] S. Wang, J. Zhang, J. Jiang, R. Liu, B. Zhu, M. Xu, Y. Wang, J. Cao, M. Li, Z. Yuan, S. Zhang, W. Huang, S. Wu, Micropor. Mesopor. Mater. 123 (2009) 349–353.
[39] E. Abi-aad, R. Bechara, J. Grimblot, A. Aboukais, Chem. Mater. 5 (1993) 793–797.
[40] J. Zhuang, W. Dai, Q. Tian, Z. Li, L. Xie, J. Wang, P. Liu, Langmuir 26 (2010) 9686–9694.
[41] D. Jiang, Y. Li, Y. Wu, P. Zhou, Y. Lan, L. Zhou, Chemosphere 89 (2012) 832–837.
[42] Q. Sun, H. Li, S. Zheng, Z. Sun, Appl. Surf. Sci. 311 (2014) 369–376.
[43] X. Hu, H. Ji, F. Chang, Y. Luo, Catal. Today 224 (2014) 34–40.
[44] G. Liu, J.A. Rodriguez, J. Hrbek, J. Dvorak, J. Phys. Chem. B 105 (2001) 7762–7770.
[45] P.O. Maksimchuk, A.A. Masalov, Yu V. Malyukin, J. Nano-Electron. Phys. 5 (2013) 01004.
[46] G. Kim, W. Choi, Appl. Catal. B: Environ. 100 (2010) 77–83.
[47] C.B. Mendive, D.W. Bahnemann, M.A. Blesa, Catal. Today 101 (2005) 237–244.
[48] D. Shao, X. Wang, Q. Fan, Micropor. Mesopor. Mater. 117 (2009) 243–248.
[49] N. Wang, L. Zhu, Y. Huang, Y. She, Y. Yu, H. Tang, J. Catal. 266 (2009) 199–206.
[50] P. Ciesla, P. Kocot, P. Mytych, Z. Stasicka, J. Mol. Catal. A: Chem. 224 (2004) 17–33.
[51] D. Wodka, E. Bielanska, R.P. Socha, M. Elzbieciak-Wodka, J. Gurgul, P. Nowak, P. Warszynski, I. Kumakiri, ACS Appl. Mater. Interfaces 2 (2010) 1945–1953.
[52] M.I. Franch, J.A. Ayllon, J. Peral, X. Domenech, Catal. Today 76 (2002) 221–233.
[53] N. Quici, M.E. Morgada, G. Piperata, P. Babay, R.T. Gettar, M.I. Litter, Catal. Today 101 (2005) 253–260.
[54] Y. Li, G. Lu, S. Li, Appl. Catal. A: Gen. 214 (2001) 179–185.
[55] Y. Wang, P. Zhang, J. Hazard. Mater. 192 (2011) 1869–1875.
[56] S. Song, J. Tu, L. Xu, X. Xu, Z. He, J. Qiu, J. Ni, J. Chen, Chemosphere 73 (2008) 1401–1406.
[57] X.Y. Wu, H.X. Qi, J.J. Ning, J.F. Wang, Z.G. Ren, J.P. Lang, Appl. Catal. B: Environ. 168 (2015) 98–104.
[58] N. Wang, L. Zhu, K. Deng, Y. She, Y. Yu, H. Tang, Appl. Catal. B: Environ. 95 (2010) 400–407.